



ELSEVIER

Nuclear Instruments and Methods in Physics Research A 478 (2002) 13–25

**NUCLEAR
INSTRUMENTS
& METHODS
IN PHYSICS
RESEARCH**
Section A

www.elsevier.com/locate/nima

Progress with micro-pattern gas detectors

R. Bellazzini*, G. Spandre, N. Lumb

INFN-Pisa, V. Livornese 1291, 56010 Pisa, Italy

Abstract

Micro-pattern gas detectors are position-sensitive proportional counters whose sense electrodes are constructed using micro-electronics, thin-film or advanced PCB techniques. The feature size attainable using these methods is of the order of a few microns and the detectors demonstrate excellent spatial resolution and fast charge collection.

We review recent progress on micro-pattern gas detectors for tracking and other cross-disciplinary applications, focussing on design principles, performance and limitations. A short list of interesting applications is discussed. © 2002 Elsevier Science B.V. All rights reserved.

Keywords: Micro-pattern; Pixelized; Imaging; Position-sensitive; Polarimeter; GEM

1. Introduction

The Micro-Strip Gas Chamber (MSGC) [1–4] is a position-sensitive proportional counter whose operational principle is analogous to that of the multi-wire proportional chamber (MWPC) [5].

Photolithographic techniques are used to build metallic strips on a supporting substrate; these electrodes are spaced at least an order of magnitude more closely than is possible for an MWPC.

The MSGC offers significant advantages in terms of spatial resolution and rate capability, thus filling the gap between cheap but rate-limited traditional gas detectors and solid-state devices, which have excellent performance but are rather expensive. MSGCs were intensively developed for the inner tracker of the CMS experiment at CERN's future LHC accelerator. Despite their clear advantages, MSGCs are generally physically

fragile devices (the substrate is usually a thin layer of glass) and rely on rather advanced technologies for their fabrication, making them still relatively expensive.

A recently introduced class of detectors exploits the procedures normally used to construct multi-layer printed-circuit boards (PCBs). The feature size obtained by this technique is larger than that attainable with photolithography but the device is cheap and robust and available in large dimensions. Examples of detectors based on advanced PCB technology are the gas electron multiplier (GEM) [6], the Micro-Groove Detector [7] and the WELL detector [8].

Examples of major experiments in which GEMs are being used are the COMPASS experiment at CERN [9] and Hera-B at DESY [10]. In the latter experiment, a GEM foil is used as a pre-amplifying stage prior to final charge amplification and collection by an MSGC. Indeed a very attractive feature of the GEM is that it allows the charge amplifying and collection structures to be completely de-coupled, allowing a high degree of

*Corresponding author. Tel.: +39-050-880-286.

E-mail address: bellazzini@pi.infn.it (R. Bellazzini).

flexibility when choosing the geometry of the read-out electrodes. Some examples of applications which exploit this feature are presented.

2. Single amplification stage—the MSGC

2.1. Detector characteristics

The MSGC is a single-stage device which has reached a mature level of technological development as a result of several years of research focussed on optimising the detectors for CMS. High rate capability and resistance to sparking were particularly important considerations. The electrode material was gold, deposited on a 300 μm thick DESAG 263 glass substrate which had been coated with a 1 μm layer of slightly conductive Pestov glass. The substrate area was $25 \times 10 \text{ cm}^2$. The anode width was 7 μm , the anode–cathode separation was 50 μm and the pitch was 200 μm . The *advanced passivation* technique (covering of the cathode edges and ends of all electrodes with a layer of polyimide) was employed to suppress streamer formation in regions of very high electric field. The gas mixture was Neon/DME, 40/60. Further details of the detector characteristics, and full explanations of the MSGC operating principle, may be found in Refs. [11,12]. There follows a description of the results of tests performed on this type of device in a high intensity hadron beam.

2.2. Experimental procedures

Thirty-two large area MSGC were tested in a 350 MeV pion beam at the Paul Scherrer Institute (PSI), Villigen, Switzerland. The particle rate was approximately 6 kHz/mm², distributed over the whole active area of the detectors; this rate was maintained for a total integrated time of 493 h. The environment to which the detectors were subjected (particle rate, probability of heavily ionising particle production, etc.) closely matched that expected for the MSGC layers foreseen at CMS; a detailed discussion of this point is given in Ref. [13]. The high intensity running period was divided into three phases: 1 week of ‘hardening’, during which previously undetected small litho-

graphic defects were expected to *burn out*; 3 weeks of continuous high intensity running with limits imposed on the acceptable number of strips lost (the CMS Milestone period); 1 week in which voltage margins would be studied by raising the S/N above the working point values.

The PSI trial was essentially a survivability test, and three main parameters were continuously checked to monitor the condition of the detectors: the signal-to-noise ratio, the number of ‘dead’ strips since the beginning of high intensity irradiation and the spark rate of each chamber. In addition, track reconstruction allowed the efficiencies of the chambers to be evaluated.

Eight of the detectors were mounted with their strips at a small stereo angle to the vertical (all other detector strips being exactly vertical). This configuration allowed two-dimensional track reconstruction, enabling us to study the imaging capabilities of the system.

2.3. Results

The average signal-to-noise ratio of all of the detectors over the Milestone period (376 integrated hours of high intensity beam) is plotted in Fig. 1.

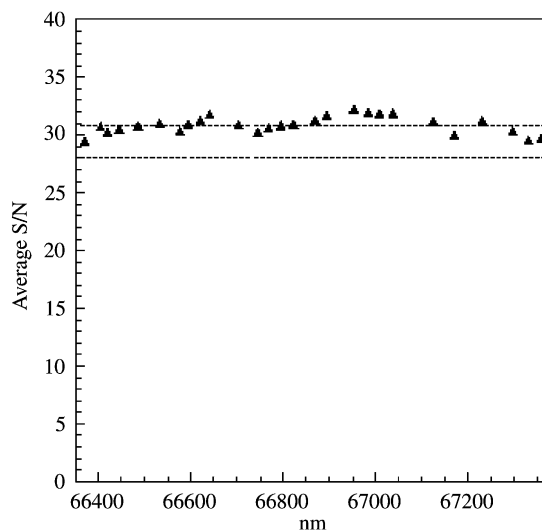


Fig. 1. Off-line S/N peak position averaged over all chambers for the Milestone period.

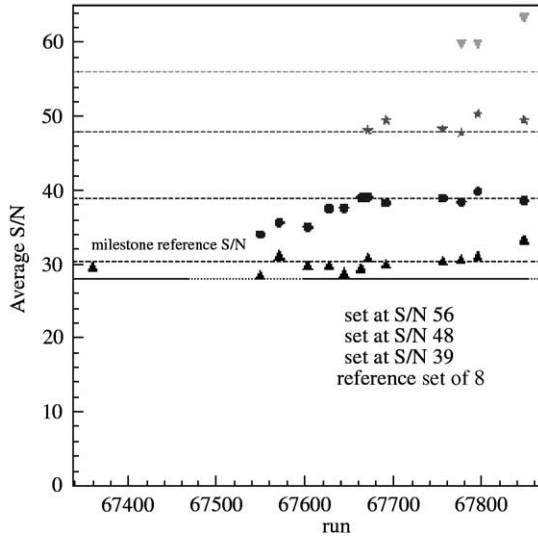


Fig. 2. Variation of average S/N with run number (margins period) for each of the different sets of detectors.

The S/N corresponding to 98% hit detection efficiency at CMS (the *working point S/N*) is 28 [12], lower horizontal line; all of the chambers were run at or above this value for the whole high intensity period. The overall average S/N value from Fig. 1 is 31, which was reached with an average cathode voltage of 515 V (drift field approximately 10 kV/cm) in the Ne/DME, 40/60 gas mixture.

There is no evidence of any gain reduction due to aging effects (the short-term variations in S/N visible in the plot are most likely due to changes in atmospheric pressure).

The stability of the detectors was also studied for S/N values significantly above the working point. While the S/N of eight reference chambers was kept at the usual value, the cathode voltages on the remaining 24 detectors were raised to give an average S/N of 39, see Fig. 2.

The voltages on half of this group of 24 were later further raised; this process was continued until six chambers were running at a S/N of 67 (2.4 times the working point value). The total duration of this study was approximately 1 week, and no degradation in chamber performance was observed. The observed strip losses for the whole

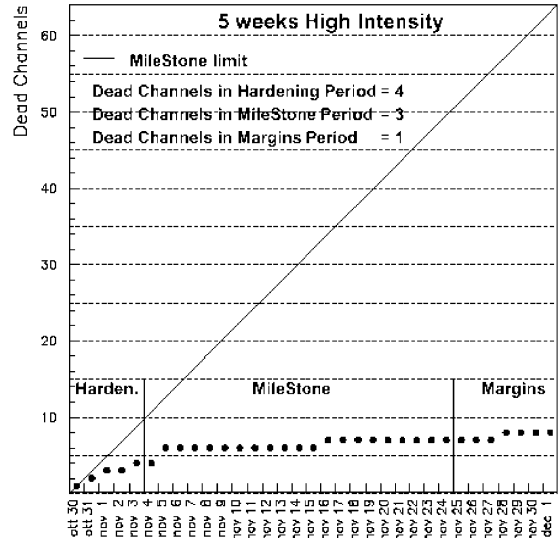


Fig. 3. Summary of all channel losses during the complete high intensity running period.

high intensity period (hardening, milestone and margins) are shown in Fig. 3.

Damaged strips were detected by comparing the noise of each strip with the start value; broken strips have a lower capacitance and hence have lower noise than an intact electrode. A total of 4 out of the 16,384 channels were lost during the hardening phase; 3 were broken in the 3 week milestone period; one further channel loss was detected during the margins study. The integrated high intensity times for these periods were 43h, 376h and 74 h, respectively. Extrapolating to 10 yr running under LHC conditions, we calculate that the expected strip loss would be 0.50%, which is 20 times lower than the CMS milestone requirement.

The low rate of strip loss was largely due to the optimized design of the detectors [11], which ensured that the spark activity in the chambers was extremely low, Fig. 4.

The plot shows the spark rate as a function of time (run number). The chambers were divided into two boxes, with 16 chambers in each box. One of the boxes was closer to the beam pipe and the spark rate was higher in this box.

The average values for both boxes are also shown in Fig. 4. The spark rate was low from the beginning (fewer than 1.5 sparks/chamber/day)

and decreased with time in both boxes, reaching a minimum of 1 spark/chamber/day in the first box and an average value over the two crates of 0.7 sparks/chamber/day at the end of the milestone period.

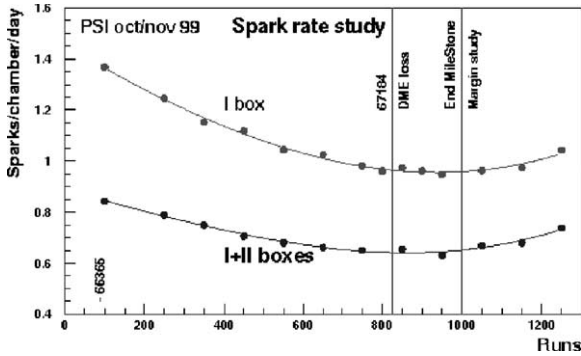


Fig. 4. Average spark rate as a function of run number for box 1 (closest to beam pipe, upper curve) and both boxes (lower curve).

The rate in both crates increased only very slightly as the voltages were increased during the margins study but was always well below the initial rate.

A detailed analysis of the tracks through the chambers was performed and it was confirmed that the hit detection efficiency at CMS using the working point voltages would be above 98% (using these voltages at PSI the chambers were fully efficient, but due consideration had to be made for the increased ballistic deficit and noise of the final CMS electronics).

Taking advantage of the eight detectors with strips oriented at a small angle to the vertical ($\alpha = 0.1$), tracks could be reconstructed in two dimensions.

Fig. 5 shows the image reconstructed after a thick brass mask with a pattern of holes drilled in it had been placed just in front of the first detector plate.

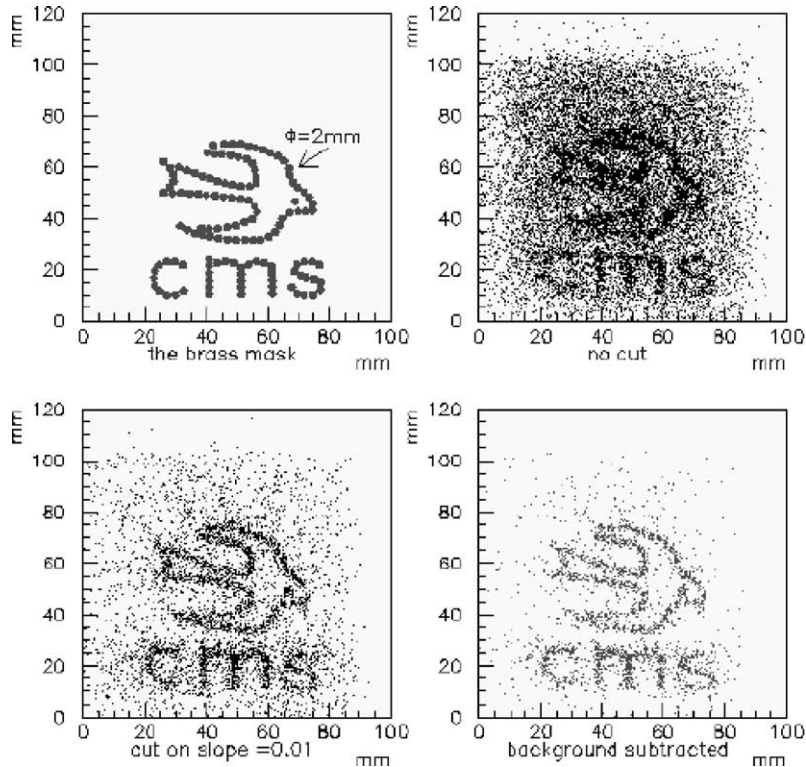


Fig. 5. The pattern of holes in the brass mask used for imaging studies was a swallow and the letters CMS. The image reconstructed from the raw data is shown together with the improved image after application of a cut on the track angle and subtraction of the Gaussian background.

3. Multi-stage devices

The GEM [6,14] consists of a layer of kapton, metallized on both sides, perforated by thousands of tiny holes. By applying a potential difference across the foil, regions of very high electric field are generated in the holes. The introduction of a drift plane parallel to the foil and a suitable gas environment results in a proportional counter capable of detecting ionising particles. One is free to choose the type of electrodes used to collect the avalanche charge. For many applications simple metal pads or strips, providing no further amplification, may be employed (see later in this paper).

In circumstances where additional gain is desirable, the charge collecting structure may itself provide further gas amplification; for example, one can use an MSGC plane. It is also possible to use additional GEM layers (double- or triple-GEM). This approach has also been suggested to mitigate the sparking problem in harsh rate hadron environment. The idea here is to reach the needed overall gain working at lower electric field in each stage. In this way, one tries to exploit the expected field-dependence of the Raether limit for sparking ($\sim 10^8$ electrons in the avalanche). We now describe some important experiments in which these ideas have been applied.

3.1. Hera-B

Hera-B is a fixed-target experiment to investigate CP-violation at the DESY facility in Hamburg. The Hera-B inner tracker is the world's largest micro-pattern detector. It consists of 184 MSGCs coupled to single GEM planes, the largest of which have dimensions $25 \times 25 \text{ cm}^2$ (total area 10 m^2), placed vertically with respect to the beam pipe.

The minimum radius from the beam pipe is 6 cm, where the particle flux reaches 10^6 particles/ cm^2/s (Fig. 6.). Indeed, data from initial running of the experiment (Fig. 7) indicates that the spark rate in the detectors is not low. However, by careful tuning of the high voltages for each

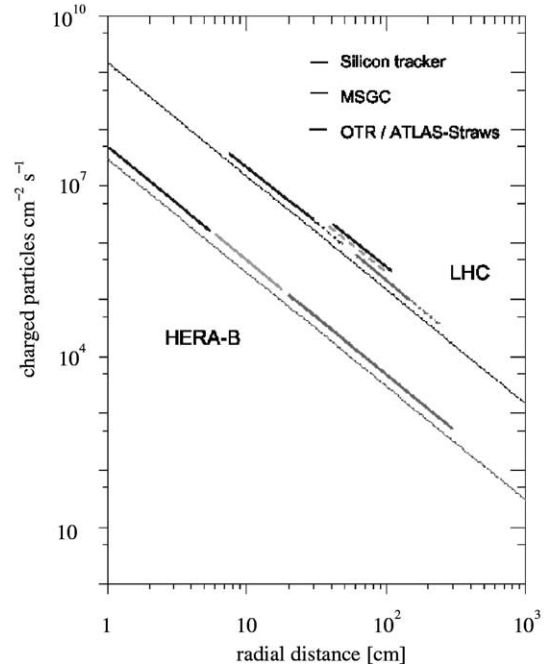


Fig. 6. Particle flux at Hera-B. The hadron environment at Hera-B provides similar detector challenges to the conditions expected at CMS taking into account the different operational radius.

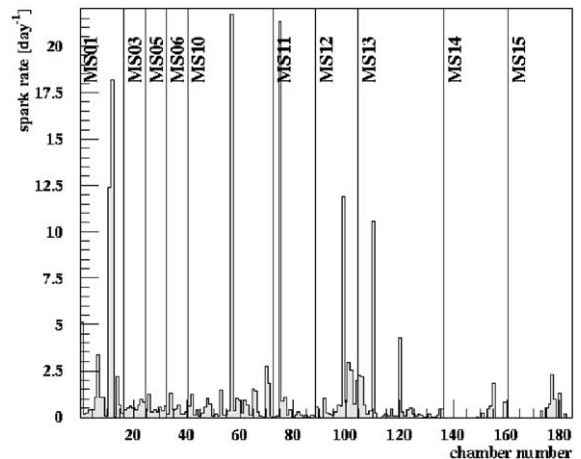


Fig. 7. Measured spark rate in GEM + MSGC at Hera-B.

individual device this problem has been kept at an acceptable level and MSGC plus GEM technology has proven to be an adequate solution for this application (Fig. 8).

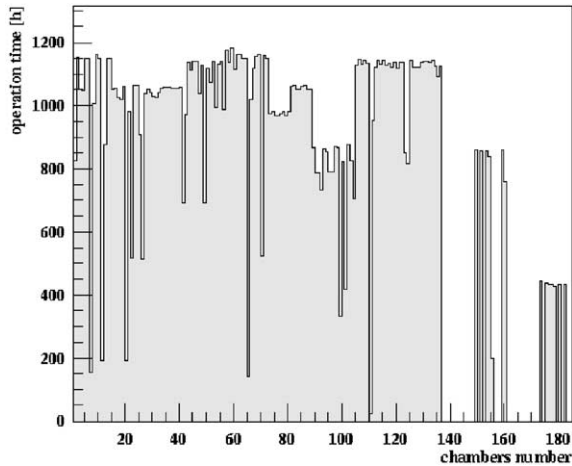


Fig. 8. Exposure time of GEM+MSGC at Hera-B.

3.2. COMPASS

COMPASS is a CERN experiment to study hadron structure and hadron spectroscopy with high intensity muon and hadron beams. The small-area tracking component of this fixed-target experiment includes detectors which utilize multiple-GEM structures [9]. Two or three large area ($31 \times 31 \text{ cm}^2$) GEM layers are spaced parallel to each other (Fig. 9), allowing gains of several tens of thousands to be achieved.

A two-dimensional (orthogonal strip) non-amplifying read-out structure is used.

Tests at PSI have shown the double GEM to be rather prone to sparking (Fig. 10) although the device is robust—after several thousand recorded sparks no damage was incurred either by the GEM foils or by the read-out electronics. The triple-GEM solution reduces the spark probability since lower voltages are required across each individual foil to achieve the same gain.

3.3. CMS forward tracker—beam test

In parallel with the tests performed at PSI on the simple (no GEM) MSGCs for the CMS tracker barrel, the forward tracker community made a thorough evaluation of the possibility of using MSGCs coupled to single GEM layers.

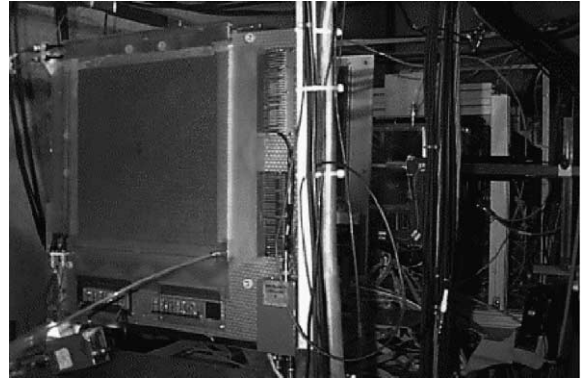


Fig. 9. The COMPASS double GEM detector at PSI.

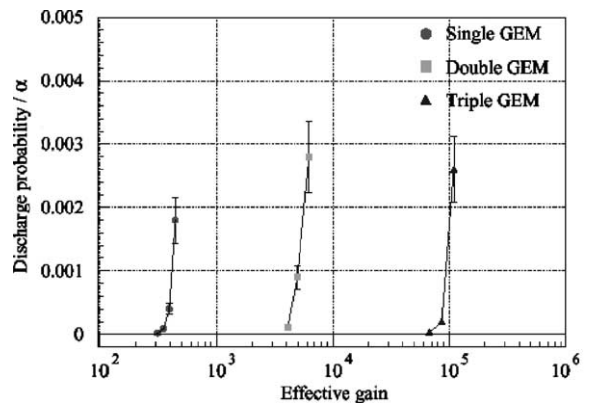


Fig. 10. Discharge probability vs. effective gain for COMPASS multiple GEMs.

This configuration allowed very high signal-to-noise ratios to be reached—see Fig. 11.

The tests successfully proved the technology to be viable for CMS, as shown by the strip loss history plot in Fig. 12. Overall strip losses were well below the challenging limit set by the CMS management.

4. GEM coupled to a pixelized read-out

The most attractive feature of the GEM is the complete separation between the amplification structure and the pick-up electrodes which allows

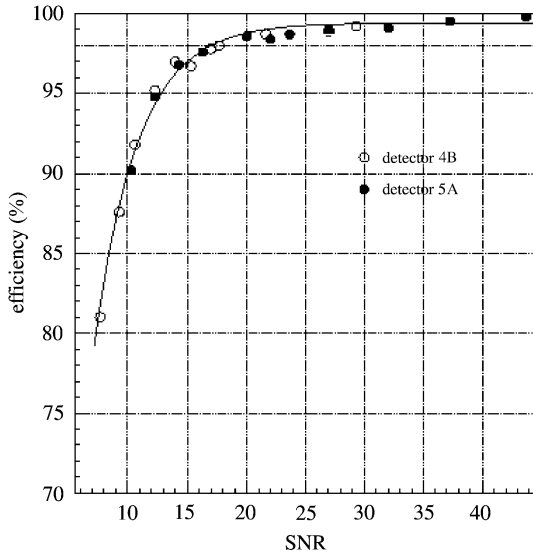


Fig. 11. Efficiency vs. S/R measured at PSI-milestone by the CMS forward chambers (GEM+MSGC).

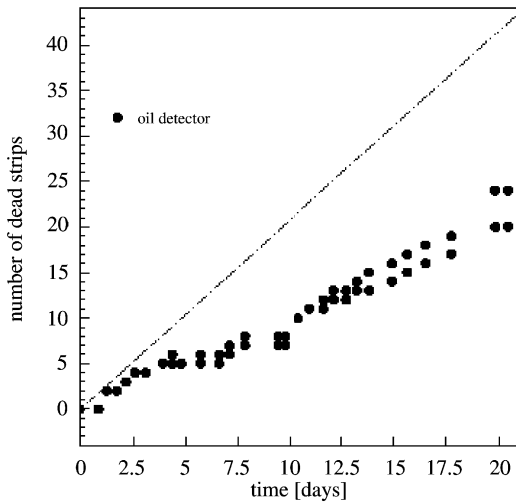


Fig. 12. Strip loss history during the 3 weeks of PSI-Milestone for the CMS Forward tracker chambers.

full flexibility on the choice of the geometry of the read-out pattern.

We have exploited this feature for two diverse applications: polarimetry of celestial X-ray sources and real-time imaging of fusion plasmas.

4.1. X-ray polarimeter for space experiments

Many galactic and extra-galactic X-ray sources are polarized. The degree of polarisation is an important consideration when constructing models for the origins of these sources.

X-ray polarimetry is a very powerful tool to explore the internal structure of compact emitting regions [15,16] otherwise inaccessible even to X-ray interferometry [17]. It could provide a direct, visual picture of the state of matter under extreme magnetic and gravitational fields by measuring the radiation polarized through the interaction with highly asymmetric matter distribution [18,19] (accretion disk) and/or magnetic field [20]. This was not possible so far because of the complexity and low sensitivity of conventional astronomical polarimeters [21–23].

We describe a new instrument based on the photoelectric effect that we have developed in collaboration with the astrophysics group of IAS–CNR of Rome lead by Enrico Costa. The polarisation information is derived from the track of the photoelectrons imaged by a finely subdivided gas detector.

The great improvement of sensitivity (at least two orders of magnitude) that can be reached with this device, will allow direct exploration of the most dramatic objects of the X-ray sky.

In the photoelectric effect with polarized photons, the electron is ejected in the direction peaked around that of the electric field of the photons.

The photoelectron interacts with the surrounding matter. It is slowed down by ionising collisions with atomic electrons and scattered by coulomb diffusion on the nuclei and eventually stopped. It leaves in the absorber a ‘track’ of electron/ion pairs from its creation to the stopping point. In the initial part of this track resides the information of the original electron direction and hence *the key* to derive the polarisation of the photon.

To resolve the track and measure the interaction point and the prime direction of the photoelectron we have developed the MPGC (Fig. 13). It consists of a gas cell with a thick detection/drift region, a thin GEM and a multi-pixel, true two-dimensional, read-out anode. The large number of fired

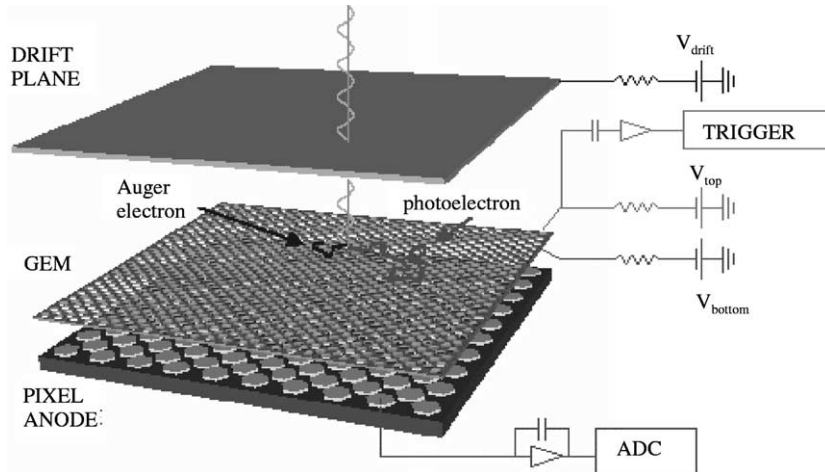


Fig. 13. The micro-pattern gas detector. The photon is absorbed at some point in the drift gap. The photoelectron track is drifted by the electric field to the GEM. This device is made of a thin ($50\ \mu\text{m}$) polyimide foil perforated by many microscopic holes, where a high electric field provides the charge amplification. Finally, the charge is collected by the pixels of the MPGC anode, each one connected to an independent electronics chain. On receiving a trigger from the GEM, all the signals are analog to digital converted, so that we have the image of the track projected on the detector plane.

pixels per track allows for good track reconstruction. Additionally, the MPGC measures the energy lost in each pixel, a quantity directly related to the kinetic energy of the electron.

We filled the MPGC with a 1 atm mixture of Ne (80%)–DME (20%). Fig. 14 shows the image of a real MPGC photoelectric track. An initial straighter part, with low ionisation density, which carries most of the information on the starting direction (and thence on the polarisation) evolves into a *skein* with high ionisation density and a completely random path.

To verify this interpretation, we let impinge on the detector, through a very thin diaphragm, photons of $5.4\ \text{keV}$ from an unpolarized source. The loci of the centroids of each track are displaced from the interaction point and located on a circular region around it, indicating that the tracks have, and retain, a significant elongation and energy loss asymmetry (Fig. 15, top). The same plot but for polarized photons is shown in Fig. 16.

From each track we reconstructed the emission angle and we built a histogram. In the case of unpolarized X-ray photons of 5.4 and $5.9\ \text{keV}$, all

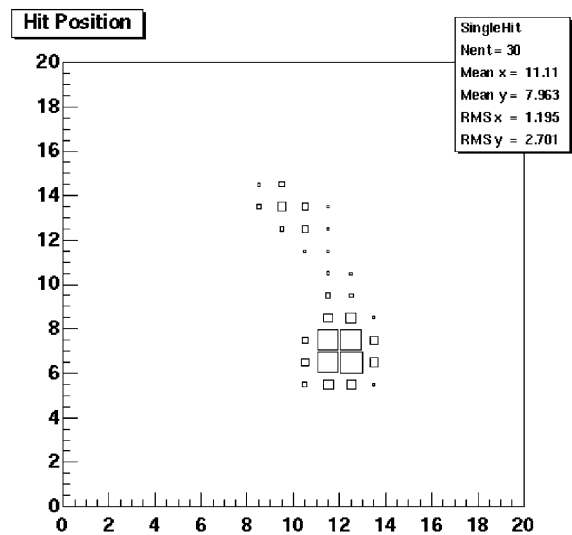


Fig. 14. Image of a real photoelectron track detected by a MPGC. Scale unit is pixel number and larger boxes correspond to a larger energy loss. Each pixel is $200\ \mu\text{m}$ wide. It is possible to recognize the beginning of the track with the Auger electron followed by the weaker ionization loss of the photoelectron (top) and the end of the track with a much larger energy loss (70% of the total charge for this specific event, bottom).

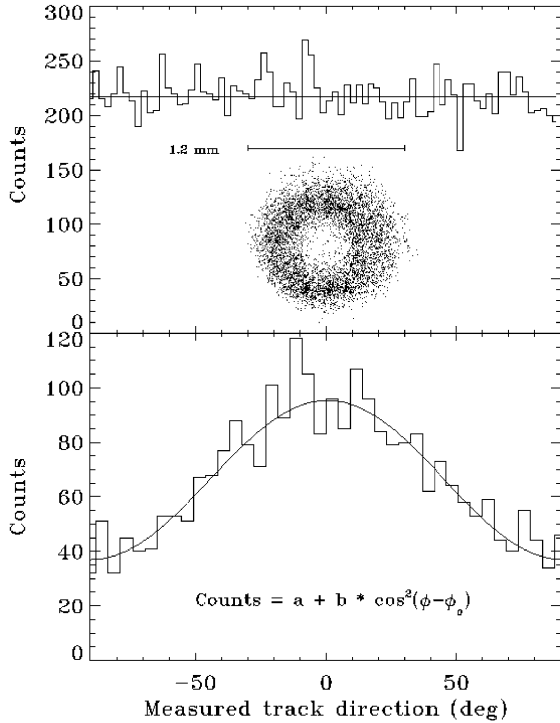


Fig. 15. Histogram of the emission angles of the photoelectron in the detector plane. The top histogram is for unpolarized photons from a Fe^{55} source. No preference in the track direction results in a histogram which is consistent with a flat curve. In the top figure, the uniform distribution of the loci of the baricenters for a 5.4 keV pencil beam of unpolarized photons are displayed, showing how tracks retain their energy loss asymmetry. The bottom histogram is for nearly 100% polarized photons from a 5.4 keV extended source. The amplitude of the \cos^2 fit to the histogram of counts is directly related to the sensitivity of a real polarimeter. The angular phase is the direction of polarization of the incoming photons. The so called *modulation factor* $(C_{\max} - C_{\min}) / (C_{\max} + C_{\min})$ is measured to be 0.44. The χ^2_{red} to the fit is 1.02, $a = 36.98 \pm 1.84$; $b = 58.43 \pm 3.57$; $\phi_0 = 0.45^\circ \pm 1.73^\circ$.

the emission angles have the same probability and the histogram is flat (Fig. 15, top).

When we irradiated the detector with an extended, nearly 100% polarized source of 5.4 keV, we found a strong angular modulation (44%) that is well modelled by the expected distribution (Fig. 15, bottom), taking into account the theoretical distribution of the photoelectron and the smearing due to scattering.

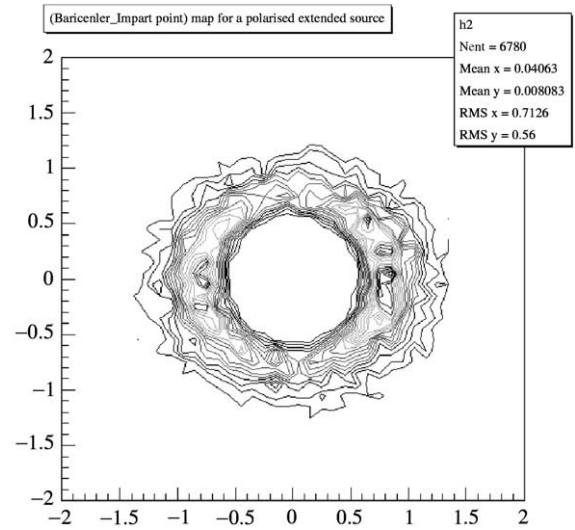


Fig. 16. The loci of the baricenters for nearly 100% polarized photons. The distribution is now clearly non-uniform.

The gas mixture used was Ne-based because, in the energy band of interest (2–10 keV) the photoelectron track is longer and fires several pixels, while retaining reasonable efficiency. Though a low Z gas is less efficient to primary photon detection, however, the scattering/slowing ratio is lower as a consequence the track is more straight and the direction of emission can be measured more precisely. Moreover, the K -edge energy is so low (0.87 keV) that the accompanying isotropic Auger electron does not blur the information on the polarisation while it helps, instead, in the identification of the impact point. The use of even lower K -edge converters together with a very fine pixel size could make low energy polarimeters (0.5–2 keV) conceivable.

This device can furthermore do simultaneously good imaging (50–100 μm), moderate spectroscopy (16% fwhm at 5.4 keV), and fast, high rate timing down to 150 eV. Moreover, being truly two-dimensional, it is non-dispersive and does not require rotation.

4.2. Real-time plasma imaging

A new diagnostic device in the soft X range (3–15 KeV) for magnetic fusion plasmas is presented.

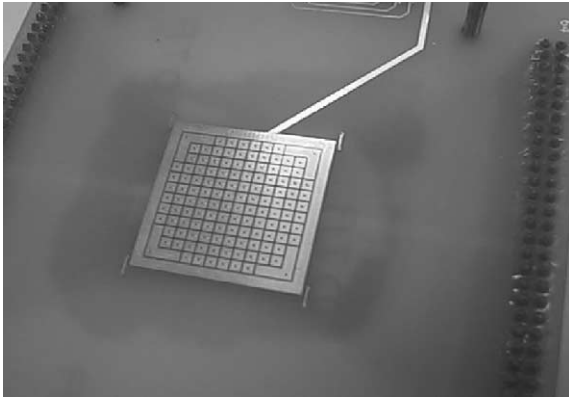


Fig. 17. Pixelized read-out board (128 pads of 2 mm²).

The instrument is again based on a GEM equipped with a true two-dimensional read-out system as shown in Fig. 17. A read-out board with 128 pixels has been designed for this purpose and coupled to a GEM detector with $2.5 \times 2.5 \text{ cm}^2$ active area. This work has been done in collaboration with the group at ENEA–Frascati lead by Danilo Pacella [24].

The device has been successfully tested with the plasma of the Frascati Tokamak Upgrade (FTU). It can be used to image plasmas at very high frequency, to study spatial distribution of X-ray emission, during many plasma processes, such as instabilities, effects of additional heating, turbulence and so on.

The GEM structure is a kapton foil 50 μm thick, with a 4 μm thick copper coating on each side. The diameter in the copper surfaces is 70 μm . The holes have a triangular pattern with a distance between the centers of 90 μm to maximize the number of openings of the GEM surface. The cathode is an aluminized mylar foil. The drift region is 4 mm high and the transfer region 1.3 mm. The collection plane is a printed circuit board with 128 square pads covering a roughly circular area. Each pad is 2 mm square.

The efficiency of collection of the primary electrons into the holes (GEM transparency) is maximized with the geometric pattern described above and the optimized ratio between the electric field of the drift gap and of the GEM foil.

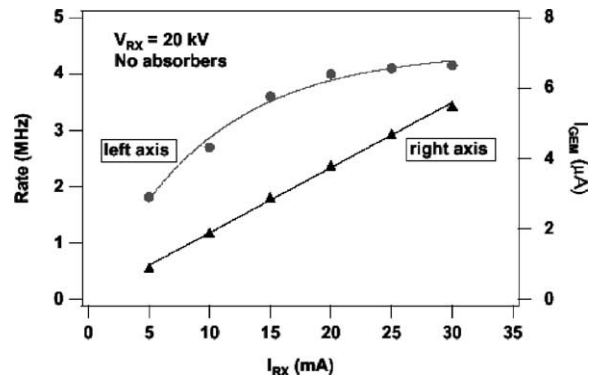


Fig. 18. Current measured on the top face of the GEM (right ordinate) and counting rate (left ordinate) on one pixel for different X-ray tube intensities without any absorber.

The field inside the hole is of the order of 10^5 V/cm , while in the transfer region it is greater than 6 kV/cm. Most of the avalanche electrons are collected on the read-out plane and generate a fast current pulse (20 ns) that can be detected by fast electronics. Each pixel is connected to a fast charge pre-amplifier (LABEN 5231), an amplifier (LABEN 5185), a low threshold discriminator (LeCroy 4608C) and a latched scaler CAMAC (LeCroy 8590). The gas mixture used in Ar 66% and DiMethylEther (DME) 33%.

The GEM operates at the gain in the interval 1000–2500. This depended on the kind of source (X-ray tube, radioactive source or plasma) and the purpose of the measurements (counting mode or spectral analysis). Drift and transfer electric fields are quite high in order to have a good match between large gains and high transparency of the GEM ($E_{\text{drift}} = 5.5 \text{ kV/cm}$) and a fast electron transfer to the read-out ($E_{\text{transfer}} = 7.5 \text{ kV/cm}$).

The whole system, detector and 128 independent electronic channels, have been tested in the laboratory to study the imaging properties at very high counting rates (up to 6 MHz/pixel).

The excellent linearity of the system response at extremely high flux rates is shown in Fig. 18 where the current in the upper face of the GEM (where part of the ions produced in the avalanche in the holes are collected) and the counts per pixel are plotted for different values of the X-ray tube current. The counting rate is linear up to

2 MHz/pixel and it is limited only by the electronic dead-time.

The result of a test of imaging capability at very high rates (> 2 MHz/pixel) is shown in Fig. 19

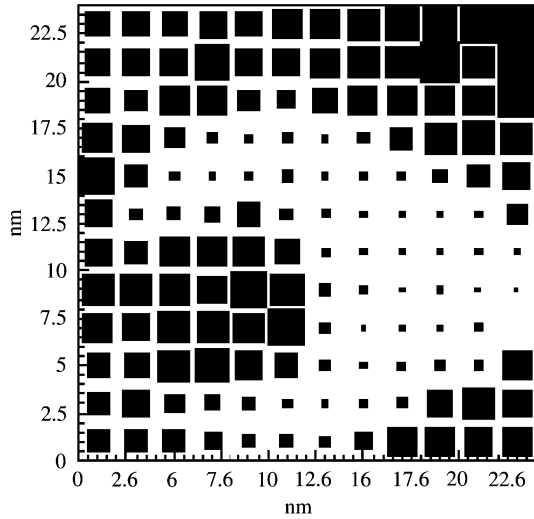


Fig. 19. Image of a stainless steel wrench placed close to the detector, at very high counting rates (~ 2 MHz/pixel, exposure time = 50 ms). In the representation, the area of the square related to each pixel is proportional to the counts.

where the shadowgraph of a wrench is represented. The area of the square pixels is proportional to the counts. The ratio between two adjacent pixels at the edge (contrast) is about 20.

FTU [25,26] is a compact, high field tokamak with toroidal field $B_t \leq 8$ T and plasma current $I_p \leq 1.6$ MA. It can operate over a wide range of densities ($0.3\text{--}3.0 \cdot 10^{20}/\text{m}^3$).

The plasma discharges last about 1.6 s with a current flat-top of 1.2 s.

To check the performance and potential of the device as diagnostic system it was mounted on FTU in a temporary and not optimized arrangement. The time history of four pixels is shown in Fig. 20. Since the detector is aligned along the central line of sight, the pixels show just small differences with the spatial position (in the start up phase the difference is a bit higher because the soft X emissivity radial profile is very peaked at the center). The signals follow the time evolutions of the soft X-ray emissions.

The drops at $t = 0.8$, $t = 0.9$, $t = 1.0$ s are caused by sudden increases of density due to D_2 multiple pellet injections.

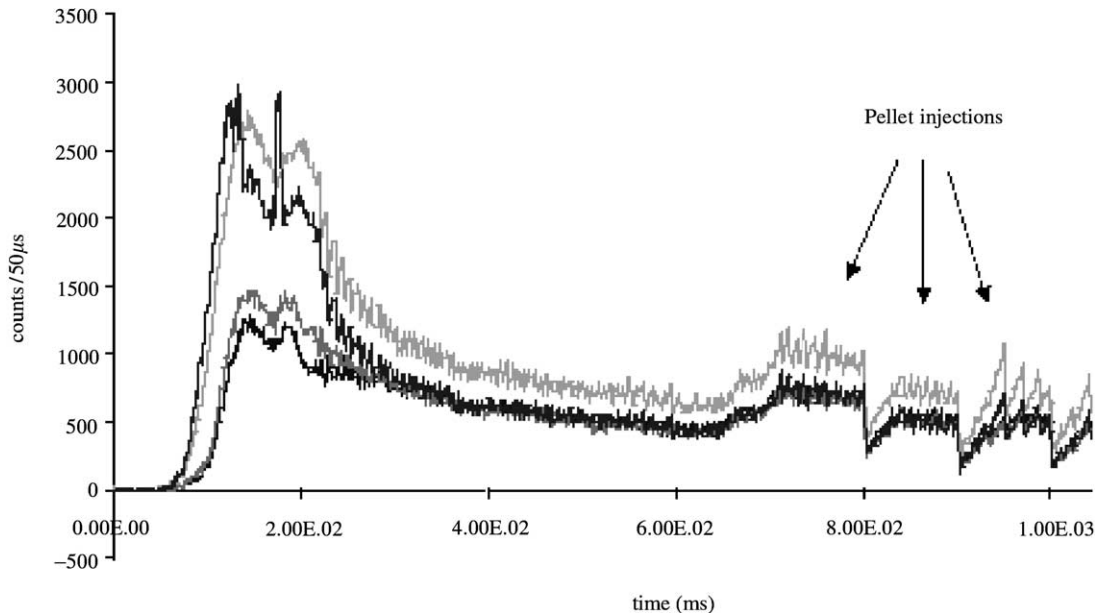


Fig. 20. Signals from four pixels of the detector aligned along the central line of sight and for an ohmic plasma. (1 KHz sampling, 3 MHz/pixel counting rate).

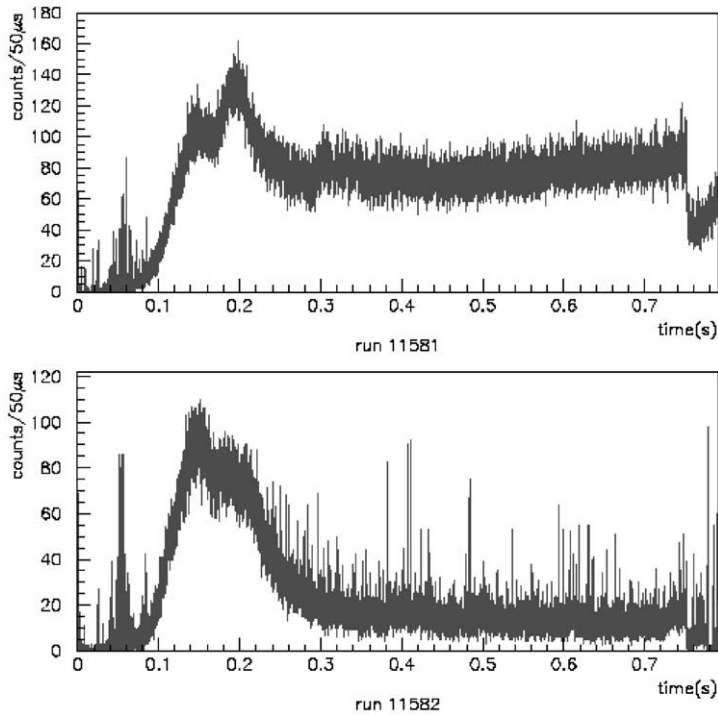


Fig. 21. Examples of fast acquisition with 20 kHz sampling frequency for two ohmic shots, normal (upper graph), aborted (lower graph). 3 MHz/pixel counting rate.

The counting rates vary from 1 (flat top) to 3 (start up phase) MHz/pixels.

Another example of ultra-fast response for two different injection runs is shown in Fig. 21. Signals were sampled at 20 kHz rate.

5. Conclusions

Micro-pattern gas detectors constitute a rapidly growing field of research which is delivering a class of device capable of filling the gap between solid state detectors and more traditional gas detectors like the MWPC. The most mature and intensively researched device in this class is the MSGC, which has been used in many diverse applications both within and outside of particle physics. A more recent development has been the introduction of detectors based on advanced printed circuit board technology. The ‘artwork’ of these devices is generally coarser than that achievable using the

micro-electronics techniques with which MSGCs are produced; there are however, distinct advantages in terms of cost and physical robustness. In the case of the GEM, in which the process of avalanche multiplication is separated from the charge collection structures, there is the additional benefit of having great flexibility in read-out design. Indeed, this approach offers one of the most exciting perspectives for future development within the field.

The performance of micro-pattern devices in currently running experiments and in many test beams has been impressive. In the case of the MSGC, it has been conclusively shown that by careful design these devices can be made to operate in high intensity hadron beams with extremely low spark rates. While higher spark rates are reported for GEM-based devices under similar conditions, the GEM foil appears to be resistant to spark damage and for certain applications represents an acceptable solution. However, the recent fall in the

price of silicon detector technology and the availability of large area silicon sensors have made the competition from solid state devices increasingly fierce, especially for tracking at hadron machines. One application where this is not the case is the detection of soft (1–10 keV) and ultra-soft (0.1–1 keV) X-rays. Gas detectors with internal gas gain have a distinct advantage here and we consider that there is great potential for micro-pattern devices in areas such as X-ray imaging. This potential is already beginning to be exploited by our group and by other researchers.

References

- [1] A. Oed, Nucl. Instr. and Meth. A 263 (1988) 351.
- [2] F. Angelini, et al., Nucl. Instr. and Meth. A 283 (1989) 755.
- [3] F. Angelini, et al., Nucl. Phys. 23A (1991) 254.
- [4] R. Bouclier, et al., Nucl. Instr. and Meth. A 323 (1992) 240.
- [5] G. Charpak, et al., Nucl. Instr. and Meth. 62 (1968) 235.
- [6] F. Sauli, Nucl. Instr. and Meth. A 386 (1997) 531.
- [7] R. Bellazzini, et al., Nucl. Instr. and Meth. A 424 (1999) 444.
- [8] R. Bellazzini, et al., Nucl. Instr. and Meth. A 423 (1999) 125.
- [9] L. Schmitt, The COMPASS Experiment, Proceedings of ICHEP98, Vancouver, 1998.
- [10] T. Hott, For the Hera-B inner tracker collaboration, presented at the 5th International Workshop on B-Physics at Hadron Machines, Los Angeles, 1997, Nucl. Instr. and Meth. A 408 (1998) 258.
- [11] CMS Technical Design Report, CERN/LHCC 98-6.
- [12] R. Bellazzini, et al., Nucl. Instr. and Meth. A. 457 (2001) 22.
- [13] M. Huhtinen, Factors to scale highly ionising particle rates in MSGC irradiation tests to the LHC radiation environment, CMS Note 1997/073.
- [14] R. Bellazzini, et al, Nucl. Instr. and Meth. A 419 (1998) 429.
- [15] J. Ogura, O. Nobuyori, Y. Kojima, Profiles and polarization properties of emission lines from relativistic disks, Publ. Astron. Soc. Japan. 52 (2000) 841.
- [16] G. Matt, A. Fabian, R. Ross, X-ray photoionized accretion discs: UV and X-ray continuum spectra and polarization, Mon. Not. R. Astron. Soc. 264 (1993) 839.
- [17] W. Cash, A. Shapley, S. Osterman, J. Marshall, Laboratory detection of X-ray fringes with grazing-incidence interferometer, Nature 407 (2000) 160.
- [18] R. Stark, P. Connors, Observational test for the existence of rotating black hole in Cyg X-1, Nature 266 (1977) 429.
- [19] P. Connors, R. Stark, Observable gravitational effects on polarised radiation coming from near a black hole, Nature 269 (1977) 128.
- [20] Y.u. Gnedin, R.A. Sunyaev, Polarization of thermal sources with magnetic field, Astron. Astrophys. 36 (1974) 379.
- [21] R. Novick, Stellar and solar X-ray polarimetry in planets, stars and nebulae studied with photopolarimetry, in: T. Gerehls (Ed.), University of Arizona Press, 1972, p. 262.
- [22] P. Soffitta, et al., Astronomical X-ray polarimetry based on photoelectric effect with microgap chamber, Nucl. Instr. and Meth. A 469 (2000) 164.
- [23] A. Timbergen, X-ray Systems in Astronomical Polarimetry, Cambridge University Press, New York, (1996) p. 120.
- [24] D. Pacella, et al., Rev. Sci. Instr. 72 (2) (2001) 1372.
- [25] R. Andreani, Fusion Eng. Des. 22 (1993) 129.
- [26] F. Alladio, et al., Plasma Phys. Controlled Fusion 36 (1994) 12B.